J. Fluid Mech. (2024), *vol*. 994, A7, doi:10.1017/jfm.2024.754

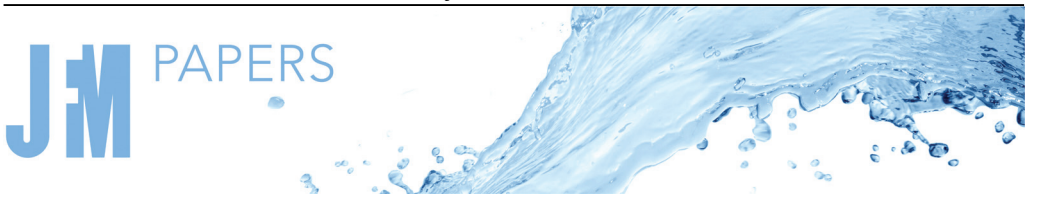

Experimental investigation of three-dimensional Rayleigh–Taylor instability of a gaseous interface

Yu Liang[1],†, **Ahmed Alkindi**[1], **Khalid Alzeyoudi**[1], **Lili Liu**[1], **Mohamed Ali**[1] and **Nader Masmoudi**[1,2]

[1]NYUAD Research Institute, New York University Abu Dhabi, Abu Dhabi 129188, UAE

[2]Courant Institute of Mathematical Sciences, New York University, 251 Mercer Street, New York, NY 10012, USA

(Received 14 November 2023; revised 1 May 2024; accepted 11 August 2024)

Validating the theoretical work on Rayleigh–Taylor instability (RTI) through experiments with an exceptionally clean and well-characterized initial condition has been a long-standing challenge. Experiments were conducted to study the three-dimensional RTI of an SF_6–air interface at moderate Atwood numbers. A novel soap film technique was developed to create a discontinuous gaseous interface with controllable initial conditions. Spectrum analysis revealed that the initial perturbation of the soap film interface is half the size of an entire single-mode perturbation. The correlation between the initial interface perturbation and Atwood numbers was determined. Due to the steep and highly curved feature of the initial soap film interface, the early-time evolution of RTI exhibits significant nonlinearity. In the quasi-steady regime, various potential flow models accurately predict the late-time bubble velocities by considering the channel width as the perturbation wavelength. Differently, the late-time spike velocities are described by these potential flow models using the wavelength of the entire single-mode perturbation. These findings indicate that the bubble evolution is influenced primarily by the spatial constraint imposed by walls, while the spike evolution is influenced mainly by the initial curvature of the spike tip. Consequently, a recent potential flow model was adopted to describe the time-varying amplitude growth induced by RTI. Furthermore, the self-similar growth factors for bubbles and spikes were determined from experiments and compared with existing studies, revealing that a large amplitude in the initial soap film interface promotes the spike development.

Key words: Buoyancy-driven instability, turbulent mixing

† Email address for correspondence: yu.liang@nyu.edu

1. Introduction

Rayleigh–Taylor instability (RTI) (Rayleigh 1883; Taylor 1950) occurs at an interface where a heavier fluid is accelerated by a lighter fluid, resulting in the formation of bubbles (lighter fluids penetrating the heavier ones) and spikes (heavier fluids penetrating the lighter ones), often culminating in a transition to turbulent flow (Zhou *et al.* 2019). RTI is recognized as a major obstacle to achieving net energy gain in inertial confinement fusion (Lindl *et al.* 2014; Betti & Hurricane 2016). Furthermore, understanding RTI and the resulting hydrodynamic mixing is crucial for comprehending supernova dynamics (Arnett 2000; Müller 2020).

The unconstrained RTI undergoes an initial regime of exponential growth, during which perturbations remain significantly smaller than their wavelength. This regime is followed by a growth saturation, resulting in quadratic growth over time within a nonlinear self-similar regime (Zhou 2017*a*,*b*). Noteworthy experiments include those conducted by Banerjee, Kraft & Andrews (2010) at an Atwood number ($A = (\rho_h - \rho_l)/(\rho_h + \rho_l)$, where ρ_h and ρ_l denote the densities of the heavier and lighter fluids, respectively) up to 0.6, by Akula & Ranjan (2016) at A up to 0.73, by Dimonte & Schneider (2000) at A up to 0.96, and others. Typical simulations involve those carried out by Cook & Dimotakis (2001), Cabot & Cook (2006), and Livescu *et al.* (2010) at $A = 0.5$, Cabot & Zhou (2013) at A up to 0.8, Livescu (2013) and Youngs (2013) at A up to 0.9, and so forth.

Most of previous experimental and numerical studies focused primarily on comprehending unconstrained RTI (Sharp 1984; Boffetta & Mazzino 2017; Zhou 2017*a*,*b*; Banerjee 2020; Livescu 2020), with only a limited portion of the literature exploring RTI arising from single-mode perturbations. However, most of the theoretical research on RTI is based on the evolution of a single-mode interface in a channel (Layzer 1955; Dimonte 2000; Oron *et al.* 2001; Goncharov 2002; Abarzhi, Nishihara & Glimm 2003; Sohn 2003; Guo & Zhang 2020; Liu, Zhang & Xiao 2023). Validating the theoretical work on the RTI through experiments with an exceptionally clean and well-characterized initial condition has been a long-standing challenge. The evolution of RTI on a single-mode perturbation constrained by walls or periodicity conditions starts with a linear regime, transitions into a quasi-steady regime (where the velocities of bubbles and spikes become time-insensitive), and is followed by a re-acceleration regime (where the velocities of bubbles and spikes increase again) (Zhang & Guo 2016).

Theoretically, several successful attempts have been made to model the single-mode RTI in different regimes. For example, the initial analysis was conducted by Rayleigh (1883) and Taylor (1950), leading to the development of linear theory. At early times, the perturbation amplitude ($a(t)$) exhibits exponential growth, as described by

$$a(t) = a_0 \cosh(\gamma t), \tag{1.1}$$

where a_0 is the initial amplitude of the interface, $\gamma = \sqrt{Agk}$, g is acceleration, and k is the perturbation wavenumber.

Moreover, Layzer (1955) developed a potential flow model for the late-time bubble velocities at $A = 1$ in the quasi-steady regime. Layzer's model was subsequently extended for arbitrary A by Goncharov (2002) and Sohn (2003), and more recently by Guo & Zhang (2020) and Liu *et al.* (2023) to include bubbles and spikes for arbitrary A. Furthermore, a buoyancy-drag model, established by Dimonte (2000) and Oron *et al.* (2001), describes the motion of bubbles and spikes by balancing inertia, buoyancy and Newtonian drag forces. This model predicts the late-time bubble velocities identical to those of Layzer (1955) and Goncharov (2002). In addition, Abarzhi *et al.* (2003) adopted a multiple harmonic approach and derived analytical solutions for the late-time bubble velocities for $A \approx 0$ and

$A \approx 1$. Overall, bubble velocities in the quasi-steady regime have been studied extensively. In contrast, the late-time spike velocities have received less attention due to the challenges posed by the large curvature and roll-up of spikes.

Numerically, Ramaprabhu & Dimonte (2005) utilized implicit large eddy simulations to simulate three-dimensional (3-D) single-mode RTI across various Atwood number scenarios. Their findings indicated that the late-time bubble velocities align more closely with the model proposed by Goncharov (2002) than with the models proposed by Sohn (2003) and Abarzhi *et al.* (2003). Ramaprabhu *et al.* (2006, 2012) further observed the re-acceleration regime at low Atwood numbers. They concluded that the secondary Kelvin–Helmholtz instability (KHI) contributes to vorticity generation, leading to bubble re-acceleration. However, they noted that this re-acceleration regime is transient, with bubbles eventually decelerating and returning to their terminal velocity over time. Furthermore, Ramaprabhu *et al.* (2006, 2012) observed that the bubble re-acceleration is completely suppressed for high-density ratios with $A \geq 0.6$.

Using direct numerical simulations, Wei & Livescu (2012) explored the two-dimensional (2-D) single-mode RTI at a low Atwood number ($A = 0.04$). They concluded that at long times and sufficiently high Reynolds numbers, the bubble's acceleration becomes stationary, indicating a period of mean quadratic growth. The authors also found good agreement between their late-time bubble velocity results and the models proposed by Oron *et al.* (2001) and Goncharov (2002), while also noting the late-time bubble re-acceleration. Recently, Bian *et al.* (2020) revisited single-mode RTI in 2-D and 3-D flows using fully compressible high-resolution simulations. They discovered that that for a sufficiently high perturbation Reynolds number, the late-time bubble re-acceleration persists and does not diminish. Additionally, their findings indicated that the re-acceleration is more likely to occur in 3-D flows than in 2-D flows, requiring lower Reynolds number thresholds.

Experimentally creating an unstable stratification of heavier fluids over lighter ones under gravity's influence is a challenge. Banerjee (2020) classified the experimental configurations in RTI studies into three categories.

(i) The accelerated interface/tank approach with lighter fluids initially over heavier fluids. For example, Lewis (1950) pioneered the use of rarefaction waves to drive the RTI of a liquid–gas interface. Morgan, Likhachev & Jacobs (2016) recently examined the single-mode RTI of various diffusive, gaseous interfaces in a rarefaction tube. Read (1984) and Youngs (1989) used a rocket rig to drive the RTI of an initially stable stratified mixture. Jacobs & Catton (1988) employed compressed air to push water downwards in a vertical tube to study 3-D RTI. Dimonte & Schneider (2000) set up a linear electric motor to accelerate a tank containing two fluids with complex acceleration histories. It is noteworthy that Wilkinson & Jacobs (2007) studied the 3-D RTI on a single-mode interface in a miscible liquid system at a low Atwood number ($A = 0.15$). The results showed that the early stage of the instability evolution is quite similar to its counterpart with a 2-D initial perturbation for the same wavenumber. In contrast to the 2-D case (Waddell, Niederhaus & Jacobs 2001), the 3-D instability eventually develops two vortices per wavelength instead of the single one found in the 2-D case. Overall, imaging the flow in an accelerated tank is challenging, and surface tension between immiscible fluids can introduce unwanted perturbations.

(ii) The situational tank approach with heavier fluids initially over lighter fluids. For example, Duff, Harlow & Hirt (1962) were the first to create a diffusive Rayleigh–Taylor unstable interface by withdrawing a barrier that separated a heavier

gas over a lighter one in a tank. However, the wake left behind the barrier introduces unwanted long-wavelength disturbances. To address this issue, Dalziel, Linden & Youngs (1999) employed a solution by stretching nylon fabric on both surfaces of the barrier to eliminate viscous boundary layers. Moreover, Huang *et al.* (2007) were the first to utilize magnetic force to precisely control the initial conditions by placing a strong paramagnetic, heavier fluid over a diamagnetic, lighter fluid. Later, this method was extended by White *et al.* (2010) using magnetorheological fluids to examine the nonlinear regime of 2-D single-mode RTI. They obtained the late-time velocities of bubbles and spikes, and reported that the spike amplitude growth rate in the $A = 1$ system does not saturate at late times, in agreement with Zhang (1998).

(iii) The flow channel approach with heavier fluids initially over lighter fluids. For example, Snider & Andrews (1994) were the pioneers to set up a water channel to study the RTI of parallel, co-flowing cold and warm streams initially separated by a thin plate. The two streams enter the channel with the same speed, mainly eliminating the KHI. However, the water tunnel experiment is limited to a low A ($\sim 10^{-3}$). To address the limitations of the water channel approach, Banerjee *et al.* (2010) set up a gas channel that uses air and helium as the two streams to study RTI mixing. The gas channel allows for a large A (~ 0.75). The flow channel approach offers extended data capture times, although the associated devices are sizable and intricate.

Overall, due to the surface tension of immiscible fluids and the diffusion of gaseous interfaces in previous RTI experiments, there is a need to develop a novel approach for creating a discontinuous gaseous interface with precise initial conditions. There is substantial evidence indicating that the flows caused by hydrodynamic instabilities may depend on initial conditions (Zhou 2017*a*,*b*). It is important that the initial perturbation shape can be described accurately in experiments. In this work, we employ soap films to create a 3-D single-mode Rayleigh–Taylor unstable interface at moderate A. The morphologies of RTI are captured by high-speed shadow photography. The variations in amplitudes, Froude numbers and self-similar factors for bubbles and spikes are measured from experiments and compared to other studies.

2. Experimental method

Soap films offer a unique and versatile platform for studying various fluid dynamics phenomena due to their ability to create thin, stable interfaces between different fluids or phases (Couder, Chomaz & Rabaud 1989). The soap film technique has been widely adopted to investigate complex phenomena such as interfacial instabilities (Ranjan *et al.* 2005; Ranjan, Oakley & Bonazza 2011), surface tension (Sane, Mandre & Kim 2018), viscoelasticity (Seiwert, Dollet & Cantat 2014), fluid–structure interactions (Zhang *et al.* 2000; Alben, Shelley & Zhang 2002), and others. The efficacy of the soap film technique in creating a discontinuous interface between SF_6 and air for Richtmyer–Meshkov instability studies has been demonstrated recently by Liu *et al.* (2018) and Liang *et al.* (2019, 2021). This technique primarily reduces the presence of additional short-wavelength disturbances and interface diffusion. In this study, we apply the soap film to create a 3-D single-mode Rayleigh–Taylor unstable interface for the first time.

As depicted in figure 1(*a*), two transparent acrylic boxes, each measuring 50.0 mm in width and length, are used. One box, 70.0 mm tall, has an open bottom, while the other, 150.0 mm tall, has an open top. The top box features two 2.1 mm diameter openings on its top cover. One opening accommodates a steel tube, secured at the centre of the box with

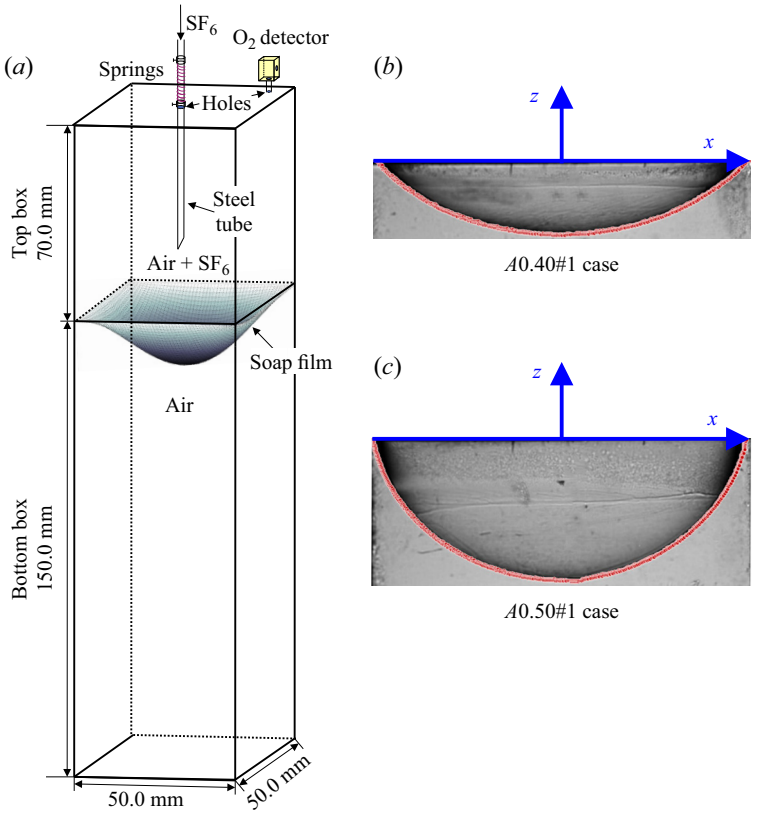

Figure 1. Schematics of the experiment set-up. (*a*). The interfacial contours extracted from the experimental images at time zero in cases (*b*) *A*0.40#1 and (*c*) *A*0.50#1, as marked in red.

springs, while the other houses an oxygen (O_2) detector positioned near one of the corners. The experimental steps are as follows.

(i) We applied a soap mixture (60 % distilled water, 20 % concentrated liquid soap, and 20 % glycerine by volume) to the bottom edges of the top box, creating a flat soap film.

(ii) The top and bottom boxes were placed vertically, connected together.

(iii) Pure SF_6 was introduced to displace the air in the top box through the steel tube, while the remaining air was expelled through the O_2 detector. To regulate the flow of SF_6 injected into the system, a gas regulator was utilized, maintaining a flow rate $0.1 \pm 0.02\ \mathrm{l\ min^{-1}}$. As a result, a homogeneous mixture of SF_6 and air was formed in the top box. The volume fraction of SF_6 (V_{SF_6}) in the mixture can be calculated as $1 - V_{O_2}/0.22$, where V_{O_2} is the volume fraction of O_2 recorded by the detector, and 0.22 is the proportion of O_2 in air.

(iv) Upon reaching a specific V_{SF_6} level, we stopped the injection of SF_6 and gently pushed the steel tube downwards at a speed of about $0.01\ \mathrm{m\ s^{-1}}$, which is significantly slower than the RTI growth rate. Moreover, different Atwood number conditions result in varying times for V_{SF_6} rising to a specific value. For instance, in the case for $A = 0.36$, the injection time for SF_6 is approximately 1.5 min; for $A = 0.46$, it is approximately 2.0 min; and for $A = 0.50$, it is approximately 2.5 min.

Case	V_{SF_6}	ρ_h (kg m^{-3})	ν (m^2 s^{-1})	A	a_0 (mm)	a_0/λ	$\sqrt{Agk_W}$ (s^{-1})
*A*0.40#1	0.33 ± 0.01	2.82 ± 0.03	8.9×10^{-6}	0.40	5.0 ± 0.1	0.10	22.2
*A*0.40#2	0.32 ± 0.01	2.80 ± 0.03	9.0×10^{-6}	0.40	5.4 ± 0.1	0.11	22.1
*A*0.43#1	0.36 ± 0.01	3.00 ± 0.02	8.5×10^{-6}	0.43	7.2 ± 0.1	0.14	22.9
*A*0.46#1	0.41 ± 0.01	3.22 ± 0.02	8.1×10^{-6}	0.46	7.2 ± 0.1	0.14	23.7
*A*0.47#1	0.44 ± 0.01	3.38 ± 0.02	7.8×10^{-6}	0.47	8.5 ± 0.01	0.17	24.2
*A*0.48#1	0.46 ± 0.01	3.47 ± 0.02	7.6×10^{-6}	0.48	8.4 ± 0.1	0.17	24.4
*A*0.48#2	0.45 ± 0.01	3.45 ± 0.02	7.6×10^{-6}	0.48	8.7 ± 0.1	0.17	24.4
*A*0.49#1	0.47 ± 0.01	3.52 ± 0.02	7.5×10^{-6}	0.49	10.1 ± 0.1	0.20	24.6
*A*0.50#1	0.48 ± 0.01	3.58 ± 0.02	7.4×10^{-6}	0.50	9.6 ± 0.1	0.19	24.7

Table 1. Physical parameters for 3-D RTI in various cases, where V_{SF_6} is the volume fraction of SF_6 in the test gas, ρ_h is the density of the test gas, ν is the weighted viscosity coefficient, A is the Atwood number, a_0 is the initial amplitude, and $\sqrt{Agk_W}$ is the classical growth rate of RTI, in which g is acceleration and k_W $(= 2\pi/W)$ is wavenumber.

(v) The sharp end of the steel tube broke the soap film, initiating the RTI driven by Earth's gravity. The time elapsed between stopping SF_6 injection and puncturing the soap film is approximately 2 s, which is much shorter than the injection time of SF_6. During this period, we continued to monitor V_{O_2} readings from the O_2 monitor. The V_{O_2} value increased by no more than 0.01 (equal to the device's measurement error) during these 2 s.

In this paper, we focus on 3-D RTI with V_{SF_6} ranging from 32 % to 48 %, corresponding to A ranging from 0.40 to 0.50. Physical parameters for 3-D RTI in different cases are provided in table 1. As V_{SF_6} increases, the surface curvature of the soap film intensifies, resulting in greater surface tension to counteract the enhanced gravity of the test gas in the top box. For example, in the *A*0.50#1 case (figure 1*c*), the soap film interface is steeper and more curved compared to that in the *A*0.40#1 case (figure 1*b*). We conducted experiments with the box width W fixed at 50.0 mm, but varied V_{SF_6} in the top box. The relationship between the initial perturbation a_0/W and the Atwood number A is depicted in figure 2. It is clear that a_0/W increases as A becomes larger, and a curve fit $a_0/W = 0.75A^2$ closely matches the experimental data. It is notable that the current set-up cannot be used to run with almost pure SF_6 since the soap film easily breaks when V_{SF_6} in the top box reaches approximately 48 %. We look forward to utilizing a mixture of SF_6 and air in the top box, and a mixture of helium and air in the bottom box. This approach has the potential to push the limits and conduct single-mode RTI experiments with high Atwood numbers in the near future.

The distinctive initial morphology of the soap film interface in shadow photography, exemplified by figures 1(*b*,*c*), facilitates the extraction of interface contours using image-processing software. The x, z coordinates of these interfacial contours at $y = 0$ for cases *A*0.40#1 and *A*0.50#1 can be obtained from the experimental images, depicted in 'real space' with x values ranging from -25.0 to 25.0 mm in figure 3(*a*). Since the initial soap film geometry represents only half of the entire sinusoidal perturbation, we acquired coordinates in the complementary half (referred to as 'virtual space' in figure 3*a*) by shifting data from x values between 0 and 25.0 mm to a range of -50.0 to -25.0 mm, and data from -25.0 to 0 mm to a range of 25.0 to 50.0 mm, while also reversing the signs of y values. Subsequently, spectrum analysis is performed on the complete sinusoidal perturbation, encompassing both real and virtual spaces, on the specific x–z plane at $y = 0$.

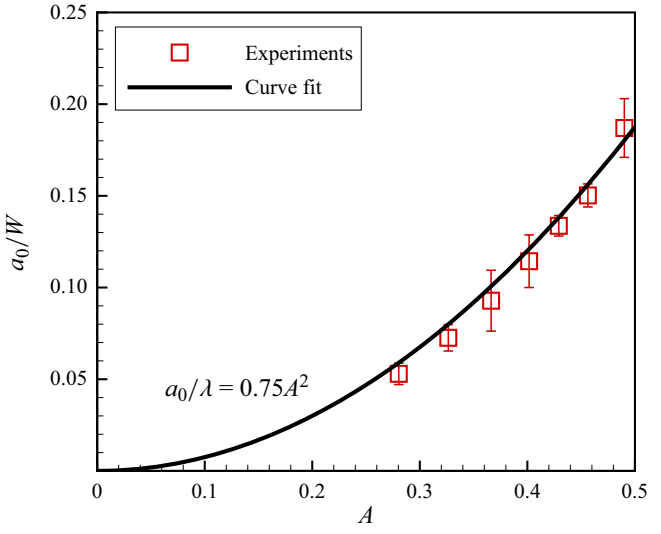

Figure 2. The variations of a_0/W versus A, with W denoting the box width.

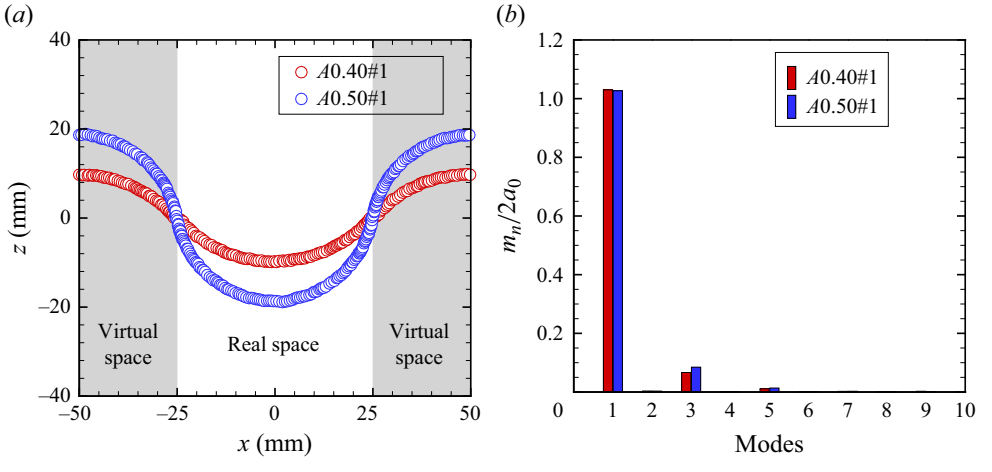

Figure 3. (*a*) The coordinates and (*b*) the initial spectrum of the initial interfacial contour in cases *A*0.40#1 and *A*0.50#1.

Figure 3(*b*) illustrates the ratio between each Fourier mode's magnitude (m_n) and the initial perturbation of a soap film interface ($2a_0$). It is clear that the short-wavelength disturbances are largely eliminated. Specifically, the fundamental mode emerges as the primary component in the initial interface perturbation, with the third-order mode exerting a secondary influence. The magnitude ratio between the third-order mode and the fundamental mode is approximately 6 %. Therefore, density loading can cause consistent and predictable deformation of the soap film, leading to a highly compact spectrum with only one Fourier mode in each horizontal coordinate direction. In comparing our initial interface spectrum with that of White *et al.* (2010) in their single-mode RTI experiments employing magnetorheological fluids, we observed a dominant mode perturbation of 1.66 mm and a secondary mode of 0.36 mm in their studies. Consequently, the magnitude ratio between the secondary mode and the dominant mode was approximately 22 %,

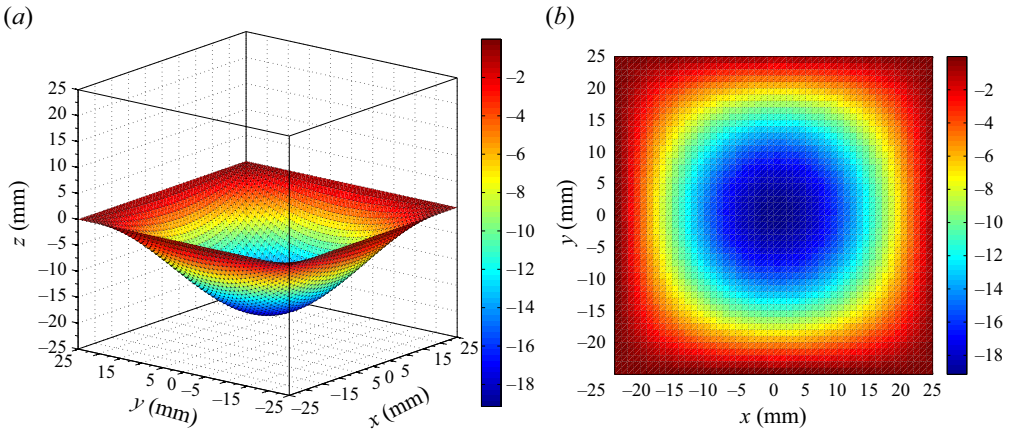

Figure 4. The initial interface perturbation in (*a* the 3-D view), and (*b*) the top view in the *A*0.50#1 case, with the colour bars indicating the values of *z*.

exceeding our experimental findings. These spectrum analysis results underscore the soap film technique's ability to generate a well-defined, reproducible 3-D single-mode Rayleigh–Taylor unstable interface.

According to the above analysis, the initial 3-D perturbation of a soap film interface can be represented as

$$z = 2a_0 \cos(\pi x/W) \cos(\pi y/W), \tag{2.1}$$

in which x and y coordinates range from -25.0 to 25.0 mm, as illustrated in figures 4(*a*,*b*). The single spike can be seen positioned at the centre, while four bubbles are situated at the corners of the channel. The flow field is captured by high-speed shadow photography, illuminated by a continuous light source. The frame rate of the high-speed camera (FASTCAM MINI WX) is 1250 fps, with shutter time 2.78 μs. The spatial resolution of images is 0.1 mm per pixel. The ambient pressure and temperature are 101.3 kPa and 293.5 ± 0.5 K, respectively.

3. Results and discussion

3.1. *Qualitative analysis*

Figures 5(*a*,*b*) illustrate the bursting of soap films in cases *A*0.40#1 and *A*0.50#1, respectively. Background subtraction has been utilized to enhance the visibility of the interfacial morphology, with detailed information provided in Appendix A. Time zero ($t = 0$) is defined as the moment when the centre of the soap film ruptures. The numbers in the images represent the dimensionless time τ (calculated as $\sqrt{Agk_W}\,t$, where g is the acceleration and equals 9.8 m s^{-2}, and k_W is the wavenumber and equals $2\pi/W = 125.7$ m^{-1} by considering W as the perturbation wavelength). As the Atwood number increases, the collapse of the soap film becomes more pronounced, leading to a longer completion time for the bursting of the soap film in the *A*0.50#1 case (7.2 ms, corresponding to a dimensionless time $\tau = 0.178$) compared to the *A*0.40#1 case (5.6 ms, corresponding to a dimensionless time $\tau = 0.125$). The soap film bursts over much shorter time scales than the entire experimental duration ($\tau = 5.0$).

When the centre of the soap film is punctured, the shadow of the soap film immediately darkens, and this dark area then spreads from the bottom to the top of the film. This

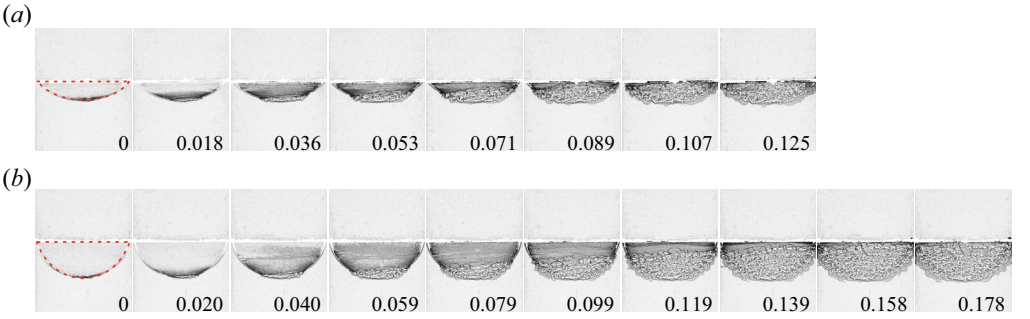

Figure 5. The bursting of soap films in (*a*) the *A*0.40#1 case and (*b*) the *A*0.50#1 case. Red dashed lines indicate the initial interface. Numbers indicate the dimensionless time $\sqrt{Agk_W}\,t$, and similar hereinafter.

darkening phenomenon reflects density fluctuations on the soap film, which are observed through shadow photography. As the soap film bursts, the soap solution gathers more in the unburst regions, leading to varying densities during the bursting process. The radial spread of soap film bursting from the point of puncture creates a broad perturbation in the surrounding gas. This rolling up of gases along the bursting surface is attributed to the KHI between SF_6 and air. Unlike the classical single-mode RTI, where bubbles and spikes evolve symmetrically in the linear regime, the early-time development of RTI in this study exhibits strong nonlinearity.

Figures 6(*a*,*b*) illustrate the evolution of the 3-D single-mode RTI in cases *A*0.40#1 and *A*0.50#1, respectively. Background subtraction maintains the outline of the initial soap film in all images. Following the rupture of the soap film, a single coherent spike penetrates downwards at the centre, while balanced bubbles form at the four corners, completing reflective symmetry ($\tau = 1.0$). This process involves the presence of small vortices. The small vortices within the top box merge into two sizeable bubbles, positioned near the left and right edges of the visualization window ($\tau = 2.0$–3.0). Concurrently, the vortices within the bottom box merge into a single, prominent spike located at the centre. As time progresses, the two bubbles continue their ascent, while the head of the spike becomes a mushroom-like shape ($\tau = 4.0$–5.0). Additionally, we observed that the boundary layer on the walls causes the heads of bubbles to slightly deviate from the side walls. Details on the boundary layer can be found in Appendix B.

3.2. *Quantitative analysis*

Time-varying dimensionless amplitudes, denoted as $\eta\ (= k_W(a - a_0))$, in various cases, are measured from experiments and presented in figure 7. The amplitude (a) is defined as the average of the bubble amplitude (a_b) and spike amplitude (a_s), both labelled in figure 6. Because the error bars for the measured amplitudes are smaller than the symbols themselves, we have chosen not to display the error bars. In the experiment, the soap film undergoes vertical deformation by a significant fraction of its width. As a result, the initial interface is steep and highly curved, potentially leading to immediate growth at a rate inconsistent with the early-time linear regime. The prediction from the linear theory ((1.1), considering k_W as the wavenumber) is indicated by a black line. It has been observed that the linear theory overestimates the experimental data beyond a dimensionless time $\tau = 0.2$. Consequently, the subsequent flow quickly transitions to a multi-modal structure after the soap film is punctured, underscoring strong nonlinearity in the early evolution of RTI in this study. Since the deformation of the initial soap film interface is directly

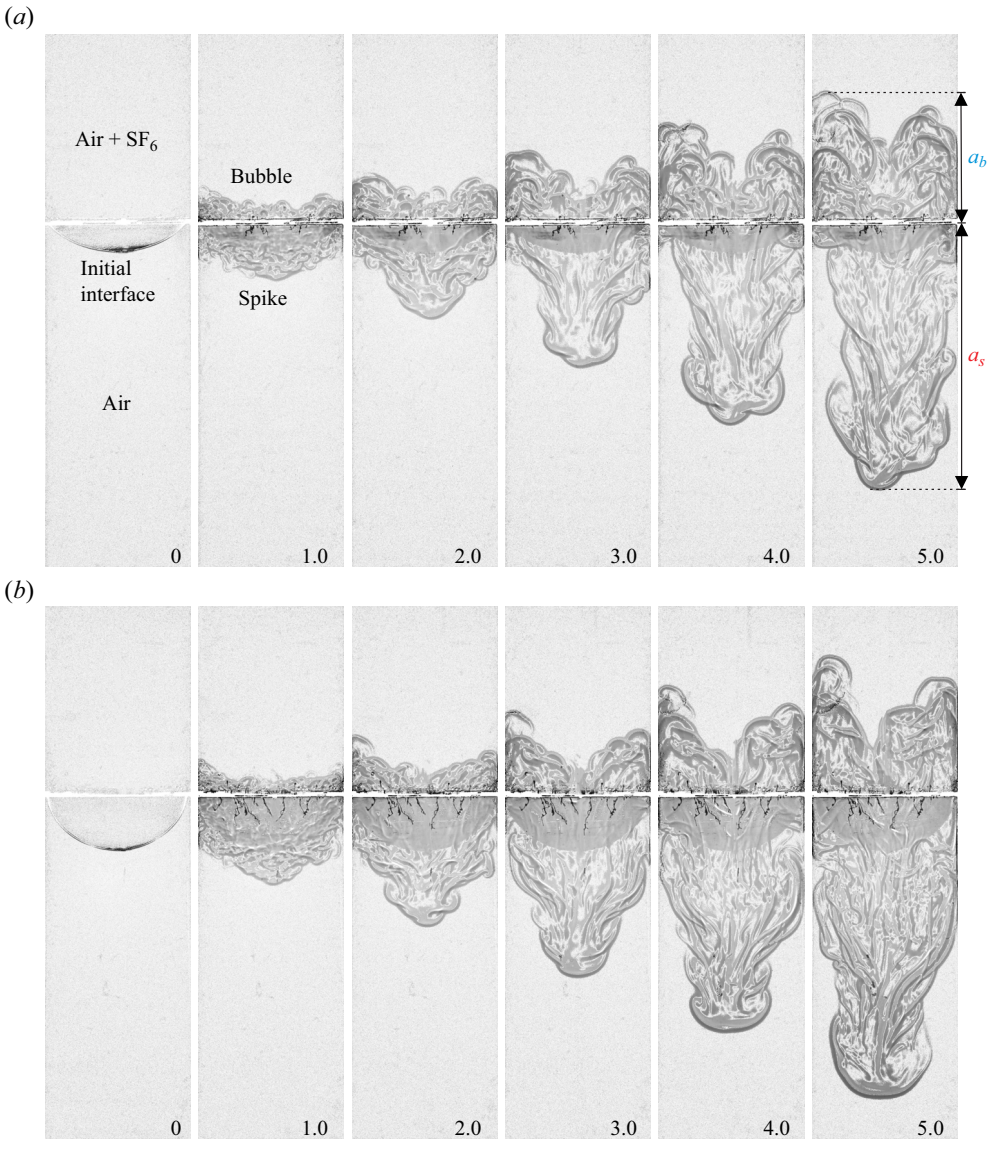

Figure 6. Shadow images of the evolution of RTI in (*a*) the *A*0.40#1 case and (*b*) the *A*0.50#1 case, with a_b and a_s denoting the amplitudes of bubbles and spikes, respectively.

influenced by the Atwood number, the departure rate from the linear regime increases with higher Atwood numbers.

The dimensionless amplitudes of bubbles η_b $(= k_W(a_b - a_0))$ and spikes η_s $(= k_W(a_s - a_0))$ deviate from each other as nonlinear effects become dominant, as shown in figure 8. Because heavier fluids exert a greater drag force on bubbles, while lighter fluids impose a smaller drag force on spikes, the bubble growth is slower than the spike growth. The time-varying amplitude growth rates of bubbles ($\dot{a}_b$) and spikes ($\dot{a}_s$) are respectively calculated by taking the first derivative of time with respect to a_b and a_s, as shown in figure 9. It is found that $\dot{a}_b$ saturates around the initial value. In contrast, $\dot{a}_s$ increases as time progresses, and then saturates after a dimensionless time $\tau = 4.5$. This

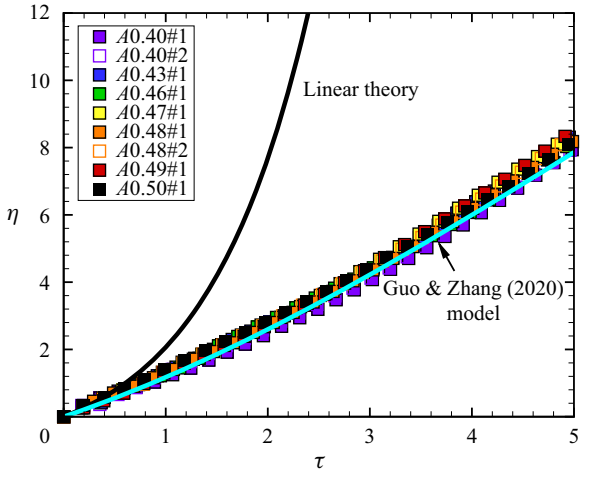

Figure 7. Time-varying dimensionless amplitudes measured from experiments. Black and cyan lines represent the predictions of the linear theory and the Guo & Zhang (2020) model at $A = 0.50$, respectively.

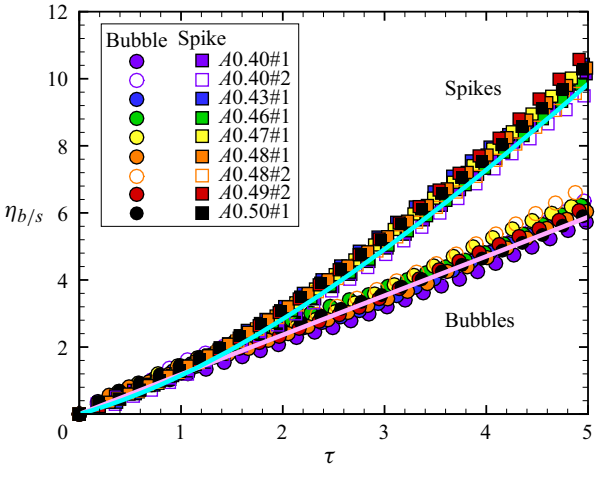

Figure 8. Time-varying dimensionless bubble amplitudes and spike amplitudes measured from experiments. Pink and cyan lines represent the predictions of the Guo & Zhang (2020) model for bubbles using the wavenumber k_W, and spikes using the wavenumber k_{2W}, at $A = 0.50$, respectively.

indicates that the development of bubbles enters the quasi-steady regime from the very beginning, while the development of spikes depends on time and enters the quasi-steady regime at a later time in our experiments.

The amplitude at which a mode transitions from exponential growth to nonlinear evolution, as anticipated by various late-time models, can be deduced by identifying the time when the linear and nonlinear modal velocities become equal (Ramaprabhu & Dimonte 2005). This method is commonly employed to model the influence of initial conditions on late-time dynamics (Layzer 1955; Dimonte 2004). The dimensionless transition bubble amplitude, denoted as ka_b^{nl}, can then be calculated using the equation

$$ka_b^{nl} = \frac{U_b}{\sqrt{Agk_W}}, \tag{3.1}$$

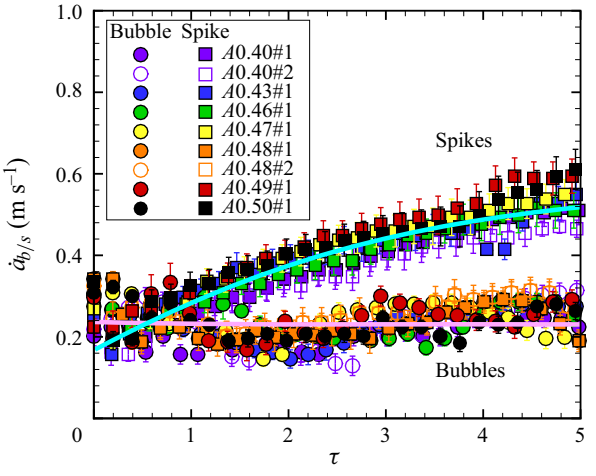

Figure 9. The time-varying amplitude growth rates of bubbles and spikes. Symbols represent experimental results in various cases. Pink and cyan lines represent the predictions of the Guo & Zhang (2020) model for bubbles using the wavenumber k_W, and spikes using the wavenumber k_{2W}, at $A = 0.50$, respectively.

where U_b represents the late-time bubble velocity. The expressions for the terminal velocities of bubbles (U_b) and spikes (U_s) in the quasi-steady regime, derived from various theoretical investigations, are detailed in table 2. Figure 10 illustrates the saturation bubble amplitude ka_b^{nl} as a function of the Atwood number A, comparing various theoretical models, numerical simulations, and experimental data (the bubble amplitude when the linear growth rate matches the measured growth rate). Our findings demonstrate that the ka_b^{nl} values obtained from experiments are consistent with multiple potential flow models (Goncharov 2002; Guo & Zhang 2020; Liu *et al.* 2023), as well as with simulation results (Ramaprabhu & Dimonte 2005). In cases with lower Atwood numbers, a longer linear regime is observed, possibly attributed to the interface maintaining an approximately sinusoidal shape even at higher amplitudes. Conversely, higher Atwood number cases tend to exhibit square wave characteristics earlier, resulting in the generation of higher-order harmonics on the interface and deviating from the linear regime.

Expressions for bubble Froude numbers (Fr_b) and spike Froude numbers (Fr_s), from various theoretical studies, are provided in table 2. According to Ramaprabhu *et al.* (2006) and Wilkinson & Jacobs (2007), Fr_b and Fr_s can be calculated as

$$Fr_{b/s} = \frac{\dot{a}_{b/s}}{\sqrt{Ag\lambda/(1 \pm A)}}. \tag{3.2}$$

Figures 11(*a*,*b*) respectively depict the plots of Fr_b and Fr_s as functions of their respective values of ξ_b ($= (a_b - a_0)/\lambda$) and ξ_s ($= (a_s - a_0)/\lambda$) for all experiments, considering the box width W as the perturbation wavelength λ, as shown with hollow symbols. The average values of Fr_b and Fr_s in various cases are presented with solid symbols. These plots also include horizontal lines representing the predictions of the various models listed in table 2.

As illustrated in figure 11(*a*), the experimental values of Fr_b exhibit oscillations around 0.60. The models proposed by Abarzhi *et al.* (2003) for $A \approx 1$ and $A \approx 0$ overestimate the experiments, while the model suggested by Sohn (2003) for $A = 0.50$ underestimates them. In contrast, the average values of Fr_b closely resemble the predictions of potential flow models proposed by Goncharov (2002) ($Fr_b \approx 0.56$), as well as those by Guo & Zhang (2020) and Liu *et al.* (2023) for $A = 0.50$. This indicates that the late-time

Model	U_b	Fr_b
Abarzhi *et al.* (2003) ($A \approx 0$)	$\left(\frac{3}{2}\right)^{3/2}\sqrt{\frac{Ag}{k}}$	$\left(\frac{3}{2}\right)^{3/2}\sqrt{\frac{1+A}{2\pi}}$
Abarzhi *et al.* (2003) ($A \approx 1$)	$\sqrt{\frac{g}{k}}\left(1-\frac{3(1-A)}{16}\right)$	$\sqrt{\frac{1+A}{2\pi A}}\left(1-\frac{3(1-A)}{16}\right)$
Goncharov (2002)	$\sqrt{\frac{2Ag}{(1+A)k}}$	$\pi^{-1/2}$
Sohn (2003)	$\sqrt{\frac{Ag}{k}}$	$\sqrt{\frac{1+A}{2\pi}}$
Guo & Zhang (2020)	$\sqrt{\frac{8[3+A+\sqrt{2}(1+A)^{1/2}]^2Ag}{(1+A)(3+A)[4(3+A)+\sqrt{2}(9+A)(1+A)^{1/2}]k}}$	$\sqrt{\frac{4[3+A+\sqrt{2}(1+A)^{1/2}]^2}{(3+A)[4(3+A)+\sqrt{2}(9+A)(1+A)^{1/2}]\pi}}$
Liu *et al.* (2023)	$(1.456-0.01A)\sqrt{\frac{Ag}{(1+A)k}}$	$(1.03-0.007A)\pi^{-1/2}$

Model	U_s	Fr_s
Goncharov (2002)	$\sqrt{\frac{2Ag}{(1-A)k}}$	$\pi^{-1/2}$
Guo & Zhang (2020)	$\sqrt{\frac{8[3-A+\sqrt{2}(1-A)^{1/2}]^2Ag}{(1-A)(3-A)[4(3-A)+\sqrt{2}(9-A)(1-A)^{1/2}]k}}$	$\sqrt{\frac{4[3-A+\sqrt{2}(1-A)^{1/2}]^2}{(3-A)[4(3-A)+\sqrt{2}(9-A)(1-A)^{1/2}]\pi}}$
Liu *et al.* (2023)	$(1.456+0.01A)\sqrt{\frac{Ag}{(1-A)k}}$	$(1.03+0.007A)\pi^{-1/2}$

Table 2. The expressions for the terminal bubble velocities (U_b) and spike velocities (U_s) in the quasi-steady regime, and the corresponding Froude numbers for bubbles (Fr_b) and spikes (Fr_s).

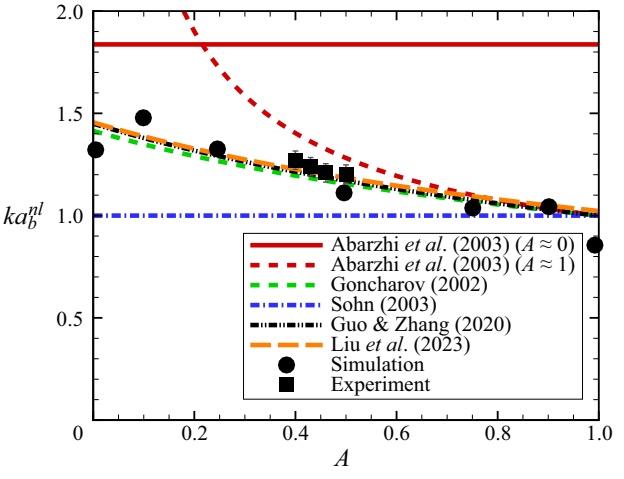

Figure 10. Nonlinear saturation bubble amplitudes ka_b^{nl} from theoretical models, simulations and experiments as a function of Atwood number A. Round symbols represent the numerical results extracted from Ramaprabhu & Dimonte (2005), and square symbols represent the present experimental results.

behaviour of bubbles is influenced mainly by the spatial constraint imposed by walls. The presence of corners in the channel may contribute to the observed oscillations in Fr_b during experiments.

In figure 11(*b*), the experimental values of Fr_s show a continuous increase over the experimental duration. This suggests that the quasi-steady regime differs between bubbles and spikes, highlighting the asymmetry between them. Consequently, the predictions of

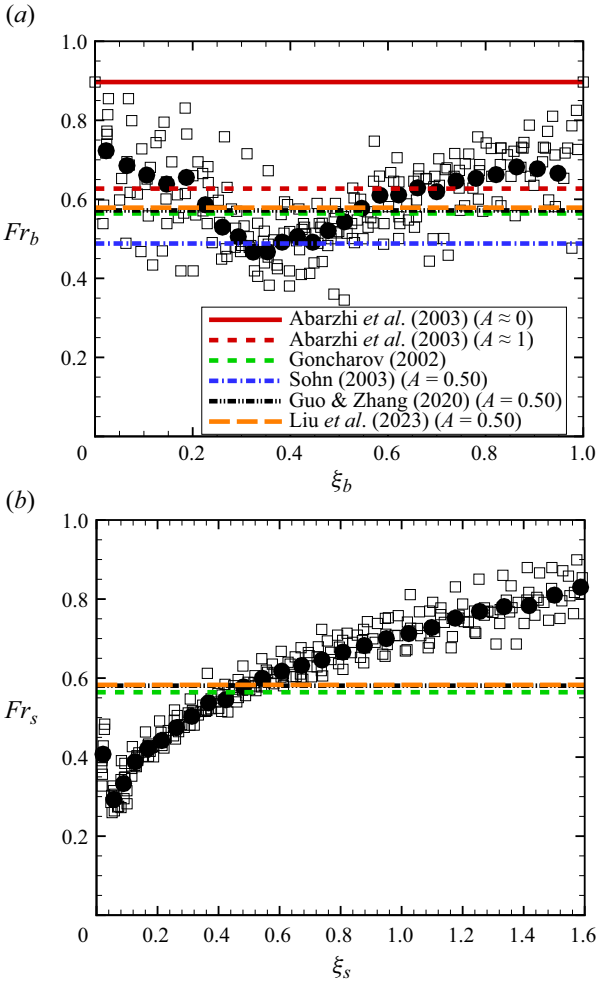

Figure 11. The variations of (*a*) the Froude numbers of bubbles Fr_b versus ξ_b, and (*b*) the Froude numbers of spikes Fr_s versus ξ_s, using the wavenumber k_W. Hollow symbols indicate experimental results in various cases, solid symbols indicate their average, and lines indicate the predictions of various models, and similarly hereinafter.

the three potential flow models (Goncharov 2002; Guo & Zhang 2020; Liu *et al.* 2023) indicating that Fr_s saturates around 0.60 underestimate the experimental observations.

The RTI experiment is conducted with a large initial amplitude, and progresses with a broad spectral signature that is dominated by a fundamental mode. The initial soap film interface in the channel is not purely symmetric, being between a single-mode case and a free-space multi-mode case. The curvature of the spike tip correlates with the entire sinusoidal perturbation, having wavelength $2W$, as shown in figure 3(*a*). Thus characterizing the spike instability with a new wavenumber k_{2W} $(= \pi/W)$ is more appropriate than using k_W $(= 2\pi/W)$, which considers only the space constrained by walls. We derive a new Froude number (Fr_s^{new}) for spikes using $2W$ as the perturbation

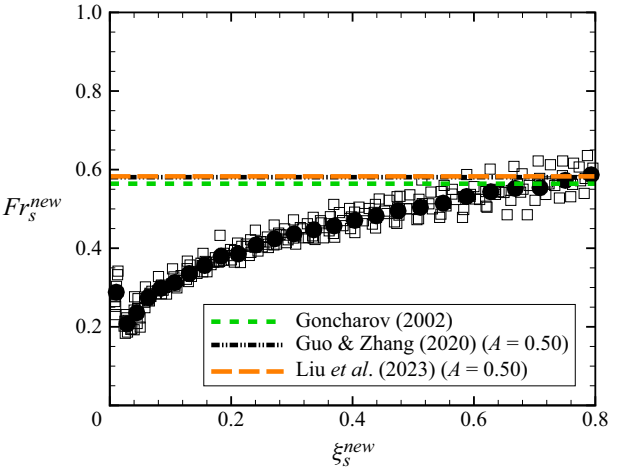

Figure 12. The variation of the new Froude numbers of spikes Fr_s^{new} versus ξ_s^{new}, using wavenumber k_{2W} $(= \pi/W)$.

wavelength, given by the expression

$$Fr_s^{new} = \frac{\dot{a}_s}{\sqrt{2AgW/(1-A)}}. \tag{3.3}$$

Figure 12 presents Fr_s^{new} plots as functions of their respective values of ξ_s^{new} $(= (a_s - a_0)/2W)$. We observe that although the experimental values of Fr_s^{new} continue to rise, they align with the predictions of potential flow models proposed by Goncharov (2002), Guo & Zhang (2020) and Liu *et al.* (2023) at a later time (corresponding to $\xi_s^{new} = 0.7$ in figure 12, and $\tau = 4.5$ in figure 9). This demonstrates that the late-time evolution of spikes is influenced primarily by the curvature of the initial spike tip.

Then we compare the experiments with the potential flow model developed by Guo & Zhang (2020) for 3-D RTI with arbitrary A using the equations

$$\ddot{a}_{b/s} = -\epsilon_{b/s} k(\dot{a}_{b/s}^2 - U_{b/s}^2), \tag{3.4}$$

where $\ddot{a}_{b/s}$ is the second derivative of time with respect to a_b or a_s, $k = k_W$ for the bubble and $k = k_{2W}$ for the spike, and $\epsilon_{b/s}$ is expressed as

$$\epsilon_{b/s} = \frac{(1 \pm A)(3 \pm A)[4(3 \pm A) + (9 \pm A)\sqrt{2(1 \pm A)}]}{2[3 + A + \sqrt{2(1 \pm A)}][4(3 \pm A) + 2\sqrt{2(1 \pm A)}(4 \mp 2A)]}. \tag{3.5}$$

The Guo & Zhang (2020) model's prediction for the average amplitude is depicted by a cyan line in figure 7. Similarly, in figure 8 (or figure 9), the Guo & Zhang (2020) model's predictions for bubble amplitudes (or bubble amplitude growth rates) and spike amplitudes (or spike amplitude growth rates) are represented by pink and cyan lines, respectively. These findings suggest that the Guo & Zhang (2020) model provides a reasonable description of the 3-D RTI studied here, particularly when taking into account that bubble evolution is affected mainly by spatial constraints from walls, while spike evolution is influenced primarily by the curvature of the initial spike tip.

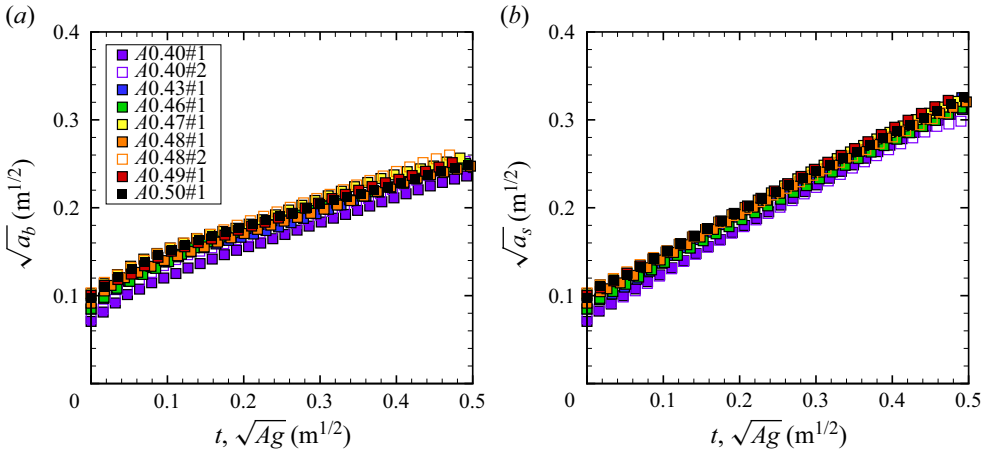

Figure 13. Measurements of self-similar factors for (*a*) bubbles α_b and (*b*) spikes α_s, determined by a linear fitting to $\sqrt{a_b}$ and $\sqrt{a_s}$ versus $t\sqrt{Ag}$.

Case	α_b	α_s
*A*0.40#1	0.041	0.172
*A*0.40#2	0.056	0.158
*A*0.43#1	0.055	0.167
*A*0.46#1	0.067	0.167
*A*0.47#1	0.053	0.171
*A*0.48#1	0.047	0.158
*A*0.48#2	0.072	0.167
*A*0.49#1	0.067	0.203
*A*0.50#2	0.058	0.195
Average	0.057 ± 0.015	0.173 ± 0.015

Table 3. The values of the self-similar factors for bubbles (α_b) and spikes (α_s) in various cases, and their averages.

Since turbulence is required for self-similarity, we calculated the maximum Reynolds number (*Re*) of the experiments as 4300 using $Re = a\dot{a}/\nu$, with ν denoting the weighted viscosity coefficient. The maximum *Re* is larger than the critical value 3700 proposed by Dalziel *et al.* (1999). Therefore, it is reasonable to discuss the self-similar factors for bubbles (α_b) and spikes (α_s) based on our experiments. As mentioned by Banerjee *et al.* (2010), one approach to determine the self-similar factors α_b and α_s is to plot $\sqrt{a_b}$ and $\sqrt{a_s}$ against $t\sqrt{Ag}$, as shown in figure 13. Subsequently, a straight line can be fitted (using the method of least squares) through the linear portion of the curve at a later time (e.g. after dimensionless time 0.4 in figure 13). Squaring the slope of this line yields an averaged value for α_b and α_s. The values of α_b and α_s in various Atwood number cases, along with their averages, are listed in table 3.

Our results indicate $\alpha_b = 0.057 \pm 0.015$ and $\alpha_s = 0.173 \pm 0.015$. In the similar *A* studies, Youngs & Read (1983) found $\alpha_b = 0.066$ and $\alpha_s = 0.086$, Kucherenko *et al.* (1991) obtained $\alpha_b = 0.055$ and $\alpha_s = 0.070$, and Dimonte & Schneider (2000) acquired $\alpha_b = 0.050$ and $\alpha_s = 0.063$. More recently, Roberts & Jacobs (2016) discovered even smaller values, such as $\alpha_b = 0.044 \pm 0.009$ and $\alpha_s = 0.057 \pm 0.014$ for the immiscible

forced experiments. Therefore, the α_b value obtained from our experiments is similar to the earlier studies, but the α_s value is noticeably higher. It is worth noting that we start with a much larger initial amplitude in the soap film interface (a_0/λ ranges from 0.10 to 0.20, as listed in table 1) compared to previous studies, resulting in strong turbulent mixing zone, which spreads into the spike (Sharp 1984). Additionally, in the current experiment, the spike spans only one wavelength, contrasting with previous unconstrained RTI studies. Because of these two possible factors, the spike develops more rapidly compared to previous experiments.

4. Conclusions

We conducted precise experiments on the three-dimensional (3-D) Rayleigh–Taylor instability (RTI) of an SF_6–air interface driven by Earth's gravity at an Atwood number (A) ranging from 0.40 to 0.50. To eliminate small-scale disturbances and diffusion layers, we employed a soap film technique to create a discontinuous gaseous interface. The relationship between the initial interface perturbation and the Atwood number was determined. Spectrum analysis revealed that the initial perturbation of the soap film interface is half the size of an entire single-mode one.

The radial propagation of soap films bursting from the point of piercing creates a broadband perturbation in the surrounding gas on both sides. Since the initial soap film interface is steep and highly curved, the early-time evolution of RTI exhibits strong nonlinearity. The experimental transition of a mode from exponential growth to nonlinear evolution in bubble amplitude aligns well with various potential flow models (Goncharov 2002; Guo & Zhang 2020; Liu *et al.* 2023) and previous simulations (Ramaprabhu & Dimonte 2005). Later, bubbles grow at a slower rate than spikes as nonlinear effects become dominant.

In the quasi-steady regime, we accurately predicted the bubble Froude number using various potential flow models (Goncharov 2002; Guo & Zhang 2020; Liu *et al.* 2023) by considering the box width W as the perturbation wavelength, indicating that the late-time evolution of bubbles is influenced mainly by the spatial constraints imposed by walls. Differently, the spike Froude number can be described effectively by these potential flow models by considering the wavelength of the entire sinusoidal perturbation $2W$, illustrating that the late-time evolution of spikes is affected primarily by the curvature of the initial spike tip. Therefore, the quasi-steady regime for bubbles and spikes is different, highlighting the asymmetry of bubbles and spikes. The recent potential flow model (Guo & Zhang 2020) was employed appropriately to describe well the time-varying perturbation growth induced by 3-D RTI.

The self-similar factors for bubbles (α_b) obtained from our experiments match previous research at similar A, but the self-similar factors for spikes (α_s) are notably larger than in previous studies. The large amplitude in the initial soap film interface with a 3-D single-mode perturbation may lead to strong turbulent mixing zone, promoting the development of spikes.

Funding. This work was supported by Tamkeen under the NYU Abu Dhabi Research Institute grant CG002.

Declaration of interests. The authors report no conflict of interest.

Author ORCIDs.
Yu Liang https://orcid.org/0000-0002-3254-7073;
Mohamed Ali https://orcid.org/0000-0001-5238-4614.

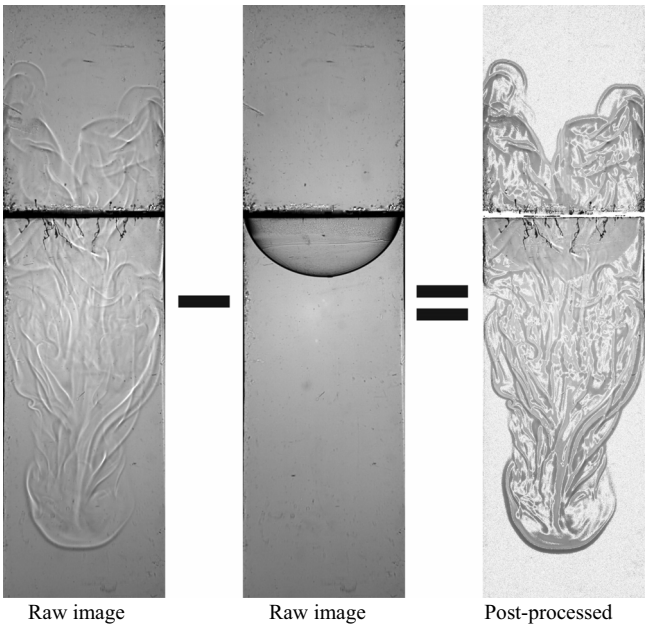

Figure 14. Sketch of the background subtraction process for experimental images.

Appendix A. Background subtraction

Throughout the sequence, we implemented background subtraction on the images, excluding the final image before the soap film is ruptured. This approach preserves the outline of the initial soap film across all images. As an example, figure 14 illustrates the background subtraction process for the image at $\tau = 5$ in the $A0.50\#1$ case. We utilized the 'Photron FASTCAM Viewer 4' software to subtract the image at $\tau = 0$ from the image at $\tau = 5$, applying a greyscale threshold from 0 to 10. This process yielded an improved image showing the interfacial morphology. Additionally, the black streaks observed near the initial interface position in the $\tau = 5$ image are shadows caused by the bursting soap film. Some bursting soap films adhered to the acrylic of the tank. Moreover, in the $\tau = 0$ image, the dark horizontal region near the initial interface signifies the boundary between the top and bottom boxes. After background subtraction, the boundary in the consecutive image is determined by subtracting the background image's boundary, resulting in a white horizontal area between bubbles and spikes.

Appendix B. Boundary layer thickness

We evaluated the thickness of the boundary layer on the walls as it may impact bubble evolution. To simplify calculations, we assumed laminar and incompressible flow throughout the experiment. Consequently, the displacement thickness of the boundary layer (δ^*) can be approximated using the formula

$$\delta^* = 1.72\sqrt{\frac{\nu a_b}{\dot{a}_b}}, \tag{B1}$$

where a_b is the bubble amplitude, $\dot{a}_b$ is the bubble amplitude growth rate, and ν is the weighted viscosity coefficient. Figure 15 shows the time-varying boundary layer thickness

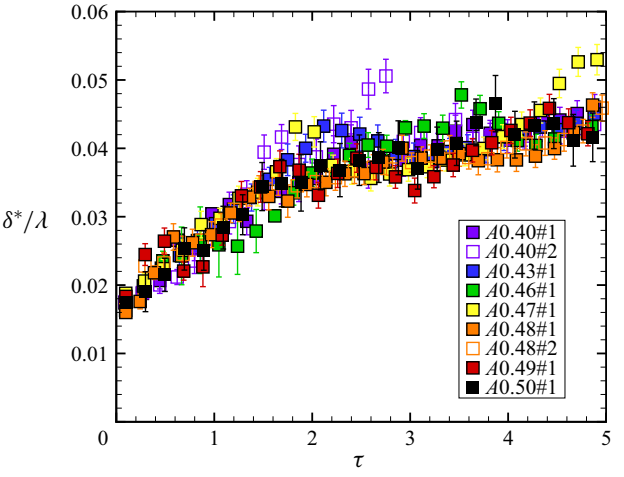

Figure 15. Time-varying displacement thickness of boundary layer on walls.

in various cases. We note a linear increase in δ^* until a dimensionless time $\tau = 2.0$, beyond which the rate of increase in δ^* levels off. Finally, δ^* attains a value 0.045 times the box width at $\tau = 5.0$. The boundary layer causes the leading edge of bubbles to slightly deviate from the side walls, as illustrated in figure 6.

References

Abarzhi, S.I., Nishihara, K. & Glimm, J. 2003 Rayleigh–Taylor and Richtmyer–Meshkov instabilities for fluids with a finite density ratio. *Phys. Lett.* A **317** (5–6), 470–476.

Akula, B. & Ranjan, D. 2016 Dynamics of buoyancy-driven flows at moderately high Atwood numbers. *J. Fluid Mech.* **795**, 313–355.

Alben, S., Shelley, M. & Zhang, J. 2002 Drag reduction through self-similar bending of a flexible body. *Nature* **420** (6915), 479–481.

Arnett, D. 2000 The role of mixing in astrophysics. *Astrophys. J. Suppl. Ser.* **127** (2), 213.

Banerjee, A. 2020 Rayleigh–Taylor instability: a status review of experimental designs and measurement diagnostics. *Trans. ASME J. Fluids Engng* **142** (12), 120801.

Banerjee, A., Kraft, W.N. & Andrews, M.J. 2010 Detailed measurements of a statistically steady Rayleigh–Taylor mixing layer from small to high Atwood numbers. *J. Fluid Mech.* **659**, 127–190.

Betti, R. & Hurricane, O.A. 2016 Inertial-confinement fusion with lasers. *Nat. Phys.* **12** (5), 435–448.

Bian, X., Aluie, H., Zhao, D., Zhang, H. & Livescu, D. 2020 Revisiting the late-time growth of single-mode Rayleigh–Taylor instability and the role of vorticity. *Physica* D **403**, 132250.

Boffetta, G. & Mazzino, A. 2017 Incompressible Rayleigh–Taylor turbulence. *Annu. Rev. Fluid Mech.* **49**, 119–143.

Cabot, W. & Zhou, Y. 2013 Statistical measurements of scaling and anisotropy of turbulent flows induced by Rayleigh–Taylor instability. *Phys. Fluids* **25** (1), 015107.

Cabot, W.H. & Cook, A.W. 2006 Reynolds number effects on Rayleigh–Taylor instability with possible implications for type Ia supernovae. *Nat. Phys.* **2** (8), 562–568.

Cook, A.W. & Dimotakis, P.E. 2001 Transition stages of Rayleigh–Taylor instability between miscible fluids. *J. Fluid Mech.* **443**, 69–99.

Couder, Y., Chomaz, J.M. & Rabaud, M. 1989 On the hydrodynamics of soap films. *Physica* D **37** (1–3), 384–405.

Dalziel, S.B., Linden, P.F. & Youngs, D.L. 1999 Self-similarity and internal structure of turbulence induced by Rayleigh–Taylor instability. *J. Fluid Mech.* **399**, 1–48.

Dimonte, G. 2000 Spanwise homogeneous buoyancy-drag model for Rayleigh–Taylor mixing and experimental evaluation. *Phys. Plasmas* **7**, 2255–2269.

Dimonte, G. 2004 Dependence of turbulent Rayleigh–Taylor instability on initial perturbations. *Phys. Rev.* E **69** (5), 056305.

DIMONTE, G. & SCHNEIDER, M. 2000 Density ratio dependence of Rayleigh–Taylor mixing for sustained and impulsive acceleration histories. *Phys. Fluids* **12**, 304–321.

DUFF, R.E., HARLOW, F.H. & HIRT, C.W. 1962 Effects of diffusion on interface instability between gases. *Phys. Fluids* **5** (4), 417–425.

GONCHAROV, V.N. 2002 Analytical model of nonlinear, single-mode, classical Rayleigh–Taylor instability at arbitrary Atwood numbers. *Phys. Rev. Lett.* **88**, 134502.

GUO, W. & ZHANG, Q. 2020 Universality and scaling laws among fingers at Rayleigh–Taylor and Richtmyer–Meshkov unstable interfaces in different dimensions. *Physica* D **403**, 132304.

HUANG, Z., DE LUCA, A., ATHERTON, T.J., BIRD, M., ROSENBLATT, C. & CARLES, P. 2007 Rayleigh–Taylor instability experiments with precise and arbitrary control of the initial interface shape. *Phys. Rev. Lett.* **99** (20), 204502.

JACOBS, J.W. & CATTON, I. 1988 Three-dimensional Rayleigh–Taylor instability. Part 2. Experiment. *J. Fluid Mech.* **187**, 353–371.

KUCHERENKO, Y.A., SHIBARSHOV, L.I., CHITAIKIN, V.I., BALABIN, S.I. & PYLAEV, A.P. 1991 Experimental study of the gravitational turbulent mixing self-similar mode. In *3rd International Workshop on the Physics of Compressible Turbulent Mixing*, pp. 427–454. Cambridge University Press.

LAYZER, D. 1955 On the instability of superposed fluids in a gravitational field. *Astrophys. J.* **122**, 1–12.

LEWIS, D.J. 1950 The instability of liquid surfaces when accelerated in a direction perpendicular to their planes. II. *Proc. R. Soc. Lond.* A **202** (1068), 81–96.

LIANG, Y., LIU, L., ZHAI, Z., DING, J., SI, T. & LUO, X. 2021 Richtmyer–Meshkov instability on two-dimensional multi-mode interfaces. *J. Fluid Mech.* **928**, A37.

LIANG, Y., ZHAI, Z., DING, J. & LUO, X. 2019 Richtmyer–Meshkov instability on a quasi-single-mode interface. *J. Fluid Mech.* **872**, 729–751.

LINDL, J., LANDEN, O., EDWARDS, J., MOSES, E. & NIC TEAM 2014 Review of the national ignition campaign 2009–2012. *Phys. Plasmas* **21** (2), 020501.

LIU, C., ZHANG, Y. & XIAO, Z. 2023 A unified theoretical model for spatiotemporal development of Rayleigh–Taylor and Richtmyer–Meshkov fingers. *J. Fluid Mech.* **954**, A13.

LIU, L., LIANG, Y., DING, J., LIU, N. & LUO, X. 2018 An elaborate experiment on the single-mode Richtmyer–Meshkov instability. *J. Fluid Mech.* **853**, R2.

LIVESCU, D. 2013 Numerical simulations of two-fluid turbulent mixing at large density ratios and applications to the Rayleigh–Taylor instability. *Phil. Trans. R. Soc.* A **371** (2003), 20120185.

LIVESCU, D. 2020 Turbulence with large thermal and compositional density variations. *Annu. Rev. Fluid Mech.* **52**, 309–341.

LIVESCU, D., RISTORCELLI, J.R., PETERSEN, M.R. & GORE, R.A. 2010 New phenomena in variable-density Rayleigh–Taylor turbulence. *Phys. Scr.* **2010** (T142), 014015.

MORGAN, R.V., LIKHACHEV, O.A. & JACOBS, J.W. 2016 Rarefaction-driven Rayleigh–Taylor instability. Part 1. Diffuse-interface linear stability measurements and theory. *J. Fluid Mech.* **791**, 34–60.

MÜLLER, B. 2020 Hydrodynamics of core-collapse supernovae and their progenitors. *Living Rev. Comput. Astrophys.* **6** (1), 3.

ORON, D., ARAZI, L., KARTOON, D., RIKANATI, A., ALON, U. & SHVARTS, D. 2001 Dimensionality dependence of the Rayleigh–Taylor and Richtmyer–Meshkov instability late-time scaling laws. *Phys. Plasmas* **8**, 2883–2889.

RAMAPRABHU, P. & DIMONTE, G. 2005 Single-mode dynamics of the Rayleigh–Taylor instability at any density ratio. *Phys. Rev.* E **71** (3), 036314.

RAMAPRABHU, P., DIMONTE, G., WOODWARD, P., FRYER, C., ROCKEFELLER, G., MUTHURAMAN, K., LIN, P.H. & JAYARAJ, J. 2012 The late-time dynamics of the single-mode Rayleigh–Taylor instability. *Phys. Fluids* **24** (7), 074107.

RAMAPRABHU, P., DIMONTE, G., YOUNG, Y.-N., CALDER, A.C. & FRYXELL, B. 2006 Limits of the potential flow approach to the single-mode Rayleigh–Taylor problem. *Phys. Rev.* E **74** (6), 066308.

RANJAN, D., ANDERSON, M., OAKLEY, J. & BONAZZA, R. 2005 Experimental investigation of a strongly shocked gas bubble. *Phys. Rev. Lett.* **94**, 184507.

RANJAN, D., OAKLEY, J. & BONAZZA, R. 2011 Shock–bubble interactions. *Annu. Rev. Fluid Mech.* **43**, 117–140.

RAYLEIGH, L. 1883 Investigation of the character of the equilibrium of an incompressible heavy fluid of variable density. *Proc. Lond. Math. Soc.* **14**, 170–177.

READ, K.I. 1984 Experimental investigation of turbulent mixing by Rayleigh–Taylor instability. *Physica* D **12** (1–3), 45–58.

ROBERTS, M.S. & JACOBS, J.W. 2016 The effects of forced small-wavelength, finite-bandwidth initial perturbations and miscibility on the turbulent Rayleigh–Taylor instability. *J. Fluid Mech.* **787**, 50–83.

SANE, A., MANDRE, S. & KIM, I. 2018 Surface tension of flowing soap films. *J. Fluid Mech.* **841**, R2.
SEIWERT, J., DOLLET, B. & CANTAT, I. 2014 Theoretical study of the generation of soap films: role of interfacial visco-elasticity. *J. Fluid Mech.* **739**, 124–142.
SHARP, D.H. 1984 An overview of Rayleigh–Taylor instability. *Physica* D **12** (1), 3–18.
SNIDER, D.M. & ANDREWS, M.J. 1994 Rayleigh–Taylor and shear driven mixing with an unstable thermal stratification. *Phys. Fluids* **6** (10), 3324–3334.
SOHN, S.I. 2003 Simple potential-flow model of Rayleigh–Taylor and Richtmyer–Meshkov instabilities for all density ratios. *Phys. Rev.* E **67**, 026301.
TAYLOR, G. 1950 The instability of liquid surfaces when accelerated in a direction perpendicular to their planes. I. *Proc. R. Soc. Lond.* A **201** (1065), 192–196.
WADDELL, J.T., NIEDERHAUS, C.E. & JACOBS, J.W. 2001 Experimental study of Rayleigh–Taylor instability: low Atwood number liquid systems with single-mode initial perturbations. *Phys. Fluids* **13** (5), 1263–1273.
WEI, T. & LIVESCU, D. 2012 Late-time quadratic growth in single-mode Rayleigh–Taylor instability. *Phys. Rev.* E **86** (4), 046405.
WHITE, J., OAKLEY, J., ANDERSON, M. & BONAZZA, R. 2010 Experimental measurements of the nonlinear Rayleigh–Taylor instability using a magnetorheological fluid. *Phys. Rev.* E **81** (2), 026303.
WILKINSON, J.P. & JACOBS, J.W. 2007 Experimental study of the single-mode three-dimensional Rayleigh–Taylor instability. *Phys. Fluids* **19**, 124102.
YOUNGS, D.L. 1989 Modelling turbulent mixing by Rayleigh–Taylor instability. *Physica* D **37** (1–3), 270–287.
YOUNGS, D.L. 2013 The density ratio dependence of self-similar Rayleigh–Taylor mixing. *Phil. Trans. R. Soc.* A **371** (2003), 20120173.
YOUNGS, D.L. & READ, K.I. 1983 Experimental investigation of turbulent mixing by Rayleigh–Taylor instability. *Tech. Rep.* O11/83. Atomic Weapons Research Establishment Report.
ZHANG, J., CHILDRESS, S., LIBCHABER, A. & SHELLEY, M. 2000 Flexible filaments in a flowing soap film as a model for one-dimensional flags in a two-dimensional wind. *Nature* **408** (6814), 835–839.
ZHANG, Q. 1998 Analytical solutions of Layzer-type approach to unstable interfacial fluid mixing. *Phys. Rev. Lett.* **81** (16), 3391.
ZHANG, Q. & GUO, W. 2016 Universality of finger growth in two-dimensional Rayleigh–Taylor and Richtmyer–Meshkov instabilities with all density ratios. *J. Fluid Mech.* **786**, 47–61.
ZHOU, Y. 2017*a* Rayleigh–Taylor and Richtmyer–Meshkov instability induced flow, turbulence, and mixing. I. *Phys. Rep.* **720–722**, 1–136.
ZHOU, Y. 2017*b* Rayleigh–Taylor and Richtmyer–Meshkov instability induced flow, turbulence, and mixing. II. *Phys. Rep.* **723–725**, 1–160.
ZHOU, Y., CLARK, T.T., CLARK, D.S., GLENDINNING, S.S., SKINNER, A.A., HUNTINGTON, C., HURRICANE, O.A., DIMITS, A.M. & REMINGTON, B.A. 2019 Turbulent mixing and transition criteria of flows induced by hydrodynamic instabilities. *Phys. Plasmas* **26** (8), 080901.